Spin injection at MgB2-superconductor/ferromagnet interface

Corentin Pfaff, S. Petit-Watelot, S. Andrieu, Ludovic Pasquier, J. Ghanbaja, S. Mangin, K. Dumesnil, T. Hauet

Spin injection at MgB_2-superconductor/ferromagnet interface

C. Pfaff[1], S. Petit-Watelot[1], S. Andrieu[1], L. Pasquier[1], J. Ghanbaja[1], S. Mangin[1], K. Dumesnil[1], T. Hauet[1*]

1.Université de Lorraine, CNRS, IJL, F-54000 Nancy, France

*thomas.hauet@univ-lorraine.fr

There is a growing interest in mixing spintronics and superconductivity to develop original energy-efficient non-volatile memory and logic devices. Researches conducted so far have mostly focused on superconductor with critical temperature T_c lower than 10K. Here, we report on the growth and characterization of $MgB_2/Ni_{80}Fe_{20}$ and MgB_2/Co bilayers where T_c of the MgB_2 layer is of the order of 30 K. Ferromagnetic Resonance was undertaken to analyze the spin pumping into MgB_2. The larger magnetization at saturation in Co, as compared to $Ni_{80}Fe_{20}$, induces a smaller spin pumping contribution to the damping when MgB_2 is normal. A Spin pumping reduction was observed for both bilayers when MgB_2 becomes superconductor and is attributed to the opening of the superconducting gap. The present results show that MgB_2 thin films could be suitable to implement superconducting spintronic at 30K which is not only relevant for future technological development, but also relaxes experimental constraints related to low-temperature investigations.

Producing and propagating polarized superconductor's quasiparticles and/or equal-spin triplet Cooper pairs, whose lifetime can exceed those of spin-polarized electrons in normal metals, may offer a way for significant energy saving in future spin-based electronics [1–3]. So far, mainly two methods have been used to study spin injection in superconductor [4]. The first method is to apply a bias voltage to force spin current propagation from a ferromagnet (F) into a superconductor (S) layer or stripe where the spin diffusion length is characterized by transport measurements [4,5]. The second method is to excite the precession of the ferromagnet's magnetization by electromagnetic waves, which produces spin pumping into an adjacent superconducting layer. The amplitude of spin angular momentum flow is characterized via the Gilbert damping parameter α measured by ferromagnetic resonance (FMR) [6–9]. A drop of α is expected to occur when the S layer turns from normal to superconducting at the critical temperature T_c because the superconducting gap opening preludes the transport of dynamically driven spin currents around the Fermi level in S [10,11], unless equal-spin triplet Cooper pairs can pump spin momentum in the superconductor [12]. Although the second method doesn't require any lithography process that may be complex, only few FMR studies have been published, including contradictory results. Several stacks including s-wave superconductors have been investigated: $TaN/Ni_{80}Fe_{20}$ ($T_c \approx 5$K) [13], Nb/ $Ni_{80}Fe_{20}$ ($T_c \approx 8$ K) [10], $NbN/Ni_{80}Fe_{20}$ ($T_c \approx 11$ K) and NbN/CoFe ($T_c \approx 9$ K)) [14]. Interestingly, the only studied S/F bilayers where F is not permalloy (NbN/CoFe [14]) did not exhibit the expected reduction of damping. This was interpreted as an effect of "dirty" S/F interface with potentially low mean free path, spin diffusion length and superconducting coherence length. Beyond s-wave superconductors, $YBa_2Cu_3O_{7-d}/Ni_{80}Fe_{20}$ ($T_c \approx 80$ K) [15] was investigated in order to benefit from the high T_c of YBCO and ensure the full opening of the gap at low temperature, which can be challenging with low-T_c materials [13]. Unfortunately, for this d-wave superconductor, the decrease of damping below T_c is partly counterbalanced by zero-gap nodes for particular directions in k-space [15].

Here, we report on the growth and the FMR investigation of $MgB_2/Ni_{80}Fe_{20}$ and MgB_2/Co bilayers. The superconducting MgB_2 layer offers T_c larger than the other s-wave superconductors, typically 30 K for films thicker than 15 nm. Using FMR technique, we observe a decrease of damping due to the superconducting gap opening as MgB_2 turns to superconducting. We characterize the spin pumping contribution to the damping and compare its amplitude in $MgB_2/Ni_{80}Fe_{20}$ and MgB_2/Co.

Single MgB_2 thin films and MgB_2/F bilayers were grown by molecular beam epitaxy under ultra-high vacuum. C-cut sapphire substrates were used and annealed at 1000 °C for at least 15 min to get clean surfaces. To avoid alloying at sapphire/MgB_2 interface [16–18], a 5 nm thick MgO (111) film was first deposited at 900°C and at a rate of 0.1 Å/s. The MgB_2 (0001) films were grown on these MgO buffer layers by evaporating Mg from an effusion cell and Boron from an electron-gun. The epitaxial process results from an interplay between the deposition temperature and the Mg to B fluxes ratio. Heating during the growth was necessary to get the MgB_2 epitaxy and was controlled by a pyrometer focused on the growing surface (using an emissivity equal to 0.25). Thus, Mg sursaturation is mandatory to get the proper stoichiometry [18]. After an exhaustive analysis of the growth by varying these 2 parameters, the best epitaxial conditions were observed for a substrate temperature close to 370 °C and using 1 Å/s and 0.1 Å/s deposition rates for Mg and B respectively, which corresponds to a Mg:B atomic ratio of 3:1. One should note that reducing the deposition temperature by only a few tens of degrees leads to the formation of Mg clusters (due to insufficient Mg desorption), while increasing it by few tens of degrees leads to multiple phases polycrystalline growth. To form S/F bilayers, F was then deposited after cooling down the sample to room temperature. We chose archetypal Co or $Ni_{80}Fe_{20}$ ferromagnetic layers, evaporated from an electron-gun with a typical deposition rate of 0.1 Å/s. Prior

to F deposition, in-situ X-ray photoemission spectroscopy confirmed that the MgB_2 surface is free from O and C, thus enabling the formation of clean $MgB_2/Ni_{80}Fe_{20}$ and MgB_2/Co interfaces.

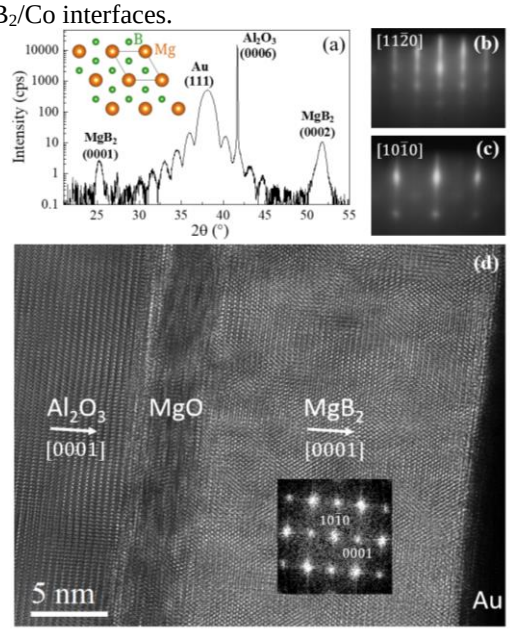

Fig. 1. (a) XRD spectrum measured on $Al_2O_3/MgO(5)/MgB_2(25)/Au(5)$ stack. In Inset is shown a scheme of two successive Mg and B planes along the MgB_2 [0001] growth direction, (b,c) RHEED patterns collected along two azimuthal directions ([11$\bar{2}$0] and [10$\bar{1}$0] MgB_2 respectively) separated by 30°. (d) HRTEM image captured along the [$\bar{1}$2$\bar{1}$0] zone axis of MgB_2. Direct Fourier transform of MgB_2 TEM image is presented in inset.

The epitaxy of both MgO(111) and MgB_2(0001) on the sapphire substrate was checked by Reflection High Energy Electron Diffraction (RHEED) performed during the growth, ex situ X-ray diffraction (XRD) using $\lambda_{Cu,K\alpha}$= 1.5406 Å and High Resolution Transmission Electron Microscopy (HRTEM). The results are shown in Fig.1. The surface hexagonal symmetry of MgB_2 (0001) was observed by RHEED (Fig.1(b) and 1(c)), and a unique crystalline phase is obtained (DRX and HRTEM). The FWHM of the MgB_2 (0002) XRD peak is 3.9°. RHEED and HRTEM observations allow us to conclude to the following epitaxial relationships [1$\bar{2}$10] Al_2O_3 (0001) // [2$\bar{1}\bar{1}$] MgO (111) // [10$\bar{1}$0] MgB_2 (0001). Note also that our process produces very flat MgB_2 upper surface (Fig.1(d)) and, so, sharp S/F interfaces as checked by x-ray reflectivity measurements on bilayers (max roughness = 0.4 ± 0.2 nm, not shown here). Co(111) was observed to grow epitaxially on MgB_2 (0001), whereas polycrystalline growth takes place for $Ni_{80}Fe_{20}$ (Fig. S1 in Suppl. Mater.). Single layers and bilayers were capped with either Au or MgO. SQUID magnetometry confirms that the few nanometers thick Co and $Ni_{80}Fe_{20}$ layers have in-plane anisotropy with no preferential direction in the plane. Their coercivity is of the order of a few mT. The Co saturation magnetization M_s is 1350 ± 50 kA/m, close to bulk value and quite insensitive to the temperature (Fig. S2). For $Ni_{80}Fe_{20}$, M_s = 710 ± 50 kA/m at 300K and increases up to 790 ± 50 kA/m at low temperature.

The critical temperatures (T_c) of single and bilayer films were deduced from resistance measurements using a QD-PPMS cryostat. They are plotted in Fig. 2 for a series of $Al_2O_3/MgO/MgB_2/Au$ films with MgB_2 thicknesses d_{MgB2} ranging from 1 nm to 91 nm. From 15 nm to 91 nm, T_c is constant around 31 K, slightly below the 39 K bulk critical temperature [18–20]. When the thickness is reduced from 15 nm to 1 nm, T_c drops and attains the temperature limit of our experimental set up, 2 K, below 5 nm. Such a reduction of T_c for low S thickness is usually explained by the increasing influence of the Cooper pair leakage towards the surrounding normal layers (inverse proximity effect), i.e. the Au layer here. In Fig.2, we compare our experimental data with the Cooper model equation $T_c(d_{MgB2}) = T_c(\infty)\exp((-d_{Cooper})/(d_{MgB2}.V))$ where $T_c(\infty)$ = 39K is the bulk MgB_2 T_c and V the interaction potential taken as 0.36 [18]. d_{Cooper} is the characteristic length of superconducting order parameter loss [21,22] usually set as the coherence length. The later, ξ_0 = 4.5±1 nm, was extracted from the field dependence of T_c using the Ginzburg-Landau equation [23], in good agreement with previous results of the literature [18,24]. One may note a significant discrepancy between the experimental dependance of T_c and Cooper's phenomenological model, which was similarly reported for high quality single crystalline MgB_2 ultra-thin films grown by HPCVD [25]. Further experimental and theoretical works are required to quantify the impact of features like interfacial strain, interfacial hybridization or Au spin-orbit coupling, on T_c.

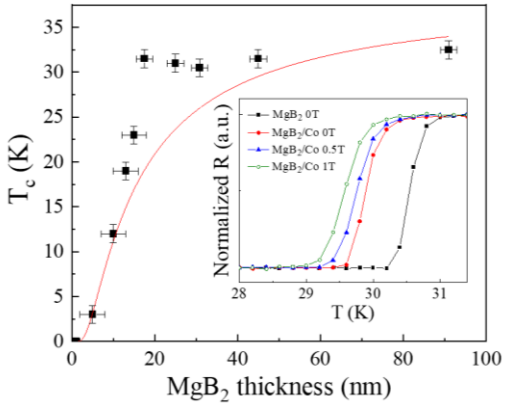

Fig. 2. MgB_2 critical temperature (black squares) as a function of the film thickness deduced from electrical resistance measurements as a function of temperature. The red curve corresponds to the theoretical variation based on the Cooper model taking account of the influence of an adjacent metallic layer on the Tc of a superconductor film. In inset are compared the R(T) for a single 25nm thick MgB_2 layer and a MgB_2(25)/Co(5) bilayer under various applied in-plane magnetic fields.

In order to estimate the impact of the F layer on the T_c of MgB_2 in MgB_2/F bilayers, a 25nm thick MgB_2 film was grown. Using a moving mask, only one part of this film was then covered by 5nm Co, while the other part remained uncovered. Finally, the whole surface was capped by Au. In inset of Fig. 2, we compare the resistance versus temperature for these two stacks (MgB_2(25)/Co(5)/Au(5) in red and MgB_2(25)/Au(5) in black). The T_c of 30.5 K for the single film is found to decrease by less than 1K when the Co layer is added, similarly to what can be observed with NbN and Nb. Interestingly, in the view of the further FMR

investigations, due to the thin film geometry and the energy cost for vortex nucleation, the application of an in-plane field up to 1T only further reduces the T_c by less than 0.5 K. The T_c of the MgB_2(25)/ $Ni_{80}Fe_{20}$(5) bilayer whose FMR investigation is presented in the following (Fig. 3) is 29.5 K.

FMR was measured by using the CoPlanar Waveguide (CPW-FMR) method [9,26] with a NanoOsc CryoFMR system in a QD-PPMS cryostat. A continuous radiofrequency (RF) Electromagnetic-field propagates along a coplanar wave guide and acts on the MgB_2/F bilayer as a magnetic harmonic exciting field, which, added to a static in-plane magnetic field, induces the precession of the F magnetization. Power loss of the transmission coefficient S_{21} is measured while sweeping the field at a fixed rf frequency (from 12 to 26 GHz). A small quasistatic oscillating field is superimposed to the DC field to allow for a lock-in detection in order to reduce experimental noise. The measured spectrum thus corresponds to the field derivative of power loss of the transmission coefficient S_{21} as a function of the static field intensity at a fixed frequency. The RF input power at the sample position is of the order of 10 dB and does not affect the sample temperature by more than 0.01K down to 5K. Power losses are maximal when the applied field matches the resonance field for a given rf excitation frequency. The FMR is characterized by the resonance field H_r and the resonance linewidth ΔH that can be extracted from a single Lorentzian derivative fit [26,27]. The resonance field at various perturbation frequencies gives access to the effective anisotropy field, the effective magnetization M_{eff} and the gyromagnetic ratio γ through Kittel formula [28]. Note that $M_{eff} = M_s - 2K_{oop}/(\mu_0 M_s)$, where K_{oop} is the out-of-plane anisotropy energy density. We find no significant in-plane anisotropy for both polycrystalline $Ni_{80}Fe_{20}$ and epitaxial Co(111). γ was fitted as 29.8 ±0.5 GHz/T from all measurements. Finally, the gilbert damping parameter α and the inhomogeneous linewidth ΔH_0 were extracted from the linear frequency dependence of ΔH in the case of a uniform mode [27]. Examples of raw data and fits are shown in Fig. S3. Note that the low frequency non-linearity in the frequency dependence of ΔH produced by two-magnon scattering, is avoided in our fitting procedure in considering only 12 to 26 GHz frequency range (inset of Fig. S3(a)). In metallic thin films as studied here, the measured damping (α) can be modeled as the sum of four main contributions [29,30]:

$$\alpha = \alpha_{int} + \alpha_{CPW} + \alpha_{eddy} + \alpha_{sp} \qquad (1)$$

The first one is the intrinsic contribution (α_{int}) of the F layer. The second and third terms arise from eddy currents either in the coplanar wave guide (α_{CPW}) or in the films (α_{eddy}), the latter being purely due to the absorption of the stray field generated by the magnetization dynamics. The last damping term (α_{sp}) corresponds to the spin damping enhancement due to spin pumping into adjacent layers, evaluated according to equation (2):

$$\alpha_{sp} = \alpha - \alpha_{ref} = \frac{g\mu_B g_{eff}^{\uparrow\downarrow}}{M_s t_F} \qquad (2)$$

where g is the Landé factor, $g_{eff}^{\uparrow\downarrow}$ is the effective spin-mixing conductance, usually independent of the temperature in metallic stacks, and t_F is the ferromagnet thickness [31,32].

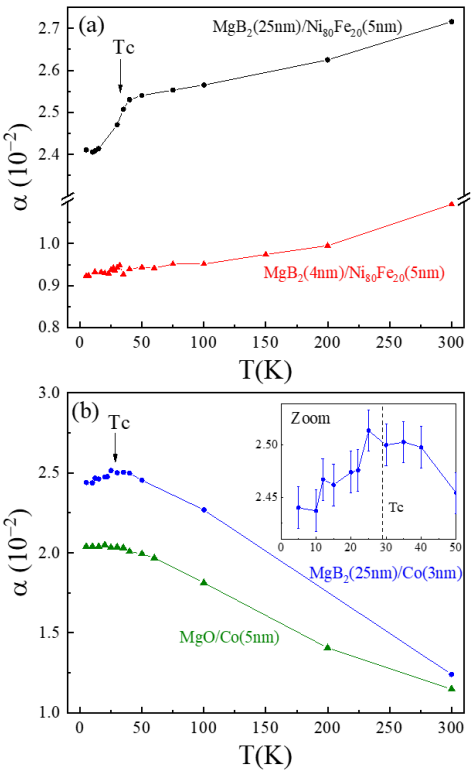

Fig. 3. Gilbert damping parameter α (extracted from the frequency dependence of the FMR linewidth), as a function of temperature T. (a) Comparison between MgB_2(25)/$Ni_{80}Fe_{20}$(5)/MgO(10) (black dots) whose critical temperature T_c is indicated by an arrow and MgB_2(4)/$Ni_{80}Fe_{20}$(5)/MgO(10) (red triangle) where MgB_2 remains a normal metal over the whole temperature range. (b) Comparison between MgB_2(25)/Co(3)/MgO(10) (blue dots) whose critical temperature T_c is indicated by an arrow and MgO/Co(5)/MgO(10) (green triangle). The inset in (b) is a zoom on the MgB_2(25)/Co(3)/MgO(10) data around Tc.

The temperature dependence of α for MgB_2(4)/$Ni_{80}Fe_{20}$(5) (red curve) and MgB_2(25)/$Ni_{80}Fe_{20}$(5) (black curve), both capped with MgO(10), are compared in Fig.3(a). As MgB_2(4) behaves as a normal metal for the whole temperature range, the MgB_2(4)/$Ni_{80}Fe_{20}$(5)/MgO(10) sample is considered as a reference to characterize the intrinsic dynamical properties of the permalloy films. M_{eff} of the two samples, extracted from FMR, only slightly increases from 720 kA/m to 780 kA/m as T varies from 300K to 5K, consistently with SQUID results (see Fig. S3(a)). It confirms that the out-of-plane anisotropy K_{oop} is negligible for all temperatures. ΔH_0 of MgB_2(25)/$Ni_{80}Fe_{20}$(5) is significantly larger than for MgB_2(4)/$Ni_{80}Fe_{20}$(5) (Fig. S4). It reveals that two-magnons scattering, crystal inhomogeneities and crystal mosaïcity, which are the main sources of inhomogeneous broadening, are stronger in the thickest bilayer, consistently with the RHEED images in Fig. S1. Note that both samples present however the same relative increase of ΔH_0 at low temperature [33]. This common temperature dependence suggests that, even if they don't have the same

crystalline quality, the inhomogeneous broadening mechanisms captured by ΔH_0 must be of similar nature in the two bilayers.

The damping of $Ni_{80}Fe_{20}(5)$ on $MgB_2(4)$ is of the order of $1.1x10^{-2}$ at 300 K and monotonically decreases down to $9x10^{-3}$ at 5 K, in agreement with data from the literature for similar layers [34]. With cooling, the permalloy resistivity and the population of thermal magnons decrease, so that spin-flip diffusion events are reduced, and the α_{int} term is lowered. A similar damping decrease was found during cooling for both $MgB_2(4)/Ni_{80}Fe_{20}(5)$ and $MgB_2(25)/Ni_{80}Fe_{20}(5)$ bilayers, at least from 300K down to T_c of the thicker MgB_2 sample. Nevertheless, the damping of the bilayer with thicker MgB_2 is significantly larger than the other one. It must originate, at least partly, from the fact that a thicker metallic layer adjacent to the F allows more absorption of the spin current generated at the interface due to spin pumping by the reduction of the spin current backflow [35]. The spin pumping, here, is not expected to vary significantly with temperature since Ms only varies a little from 300K to 5K. No experimental determination of MgB_2 spin flip length (λ_{sf}) has been reported yet. From our data set, we can deduce that λ_{sf} in MgB_2 is larger than 4 nm. Otherwise, the spin pumping contribution to the damping would have been already maximum with MgB_2 (4nm) and the damping value would have been the same in the two samples. The difference of crystallinity, characterized by RHEED in Fig. S1, can be a second source of α difference, through a difference of α_{int}. If it is the case, as the various mechanisms of α_{int} have different temperature dependence, the constant difference of α between the two samples above Tc suggests that the same α_{int} mechanisms must occur in the two samples but with different amplitude. Finally, radiative contributions to the damping, α_{eddy} and α_{CPW}, were estimated, when MgB_2 is normal, to be at most of the order of 10^{-5} and 10^{-4} respectively, i.e. two orders of magnitude smaller than the difference of α between the two samples (See Fig.S2). So, these last two contributions are negligible compared to a difference of spin pumping and α_{int}.

The damping parameter of $MgB_2(25)/Ni_{80}Fe_{20}(5)$ drops below T_c ($\Delta\alpha^S = 1.4x10^{-3}$). Since the reference sample does not show the same drop, this later does not originate from a variation of α_{int} in $Ni_{80}Fe_{20}$. Besides, the radiative contributions to the damping, α_{eddy} and α_{CPW}, are still one or two orders of magnitude smaller than $\Delta\alpha^S$ (see Fig.S2). As a consequence, we can conclude that only a change in α_{sp} can account for the $\Delta\alpha^S$ decrease observed for the thicker MgB_2 sample below T_c. One can relate $\Delta\alpha^S$ to the opening of the superconducting gap in MgB_2 since a plateau of α is found below half T_c (15K), consistently with the saturation of the gap predicted in the BCS theory [36]. It is to be noted that, as in previous report on S/F with metallic F [10,11,13], no peak of α is observed immediately below Tc. Such a peak of damping, predicted in Ref. [37,38], would be due to an enhancement of quasiparticle density-of-states. In the present case of a metallic F, the interface exchange interaction may strongly or even completely suppress the superconducting gap at the MgB_2/F interface and so may kill the mechanism for simultaneous spin-flip scattering of a quasiparticle and magnon annihilation [39]. It is also to be noted that $\Delta\alpha^S$ is only 10% of the difference of damping above Tc between $MgB_2(4)/Ni_{80}Fe_{20}(5)$ and $MgB_2(25)/Ni_{80}Fe_{20}(5)$ bilayer. The small amplitude of $\Delta\alpha^S$ could first suggest that the variation in α_{int} is the main source of damping difference between the two samples above Tc. It could also indicate that the gap opening does not totally preclude spin current absorption in the tested samples. Spin-pumping by quasi-particles or scattering within the proximitized region may still allow spin relaxation when MgB_2 is superconductive. Finally, less likely, it could also reveal the appearance of a hidden additional positive damping contribution below T_c which would compete with the gap-induced loss of damping. For instance, the transition of MgB_2 from normal metal to superconducting could lead to an increase of α_{CPW} since the magnetic field generated by the magnetization dynamics is expulsed closer to the CPW.

Similar studies of the temperature dependences of damping were performed on $MgB_2(25)/Co(3)$ and $MgB_2(25)/Co(5)$, and compared with the reference sample $MgO(5)/Co(5)/MgO(10)$. Here, as shown in Fig. S1, the reference sample does not required any thin MgB_2 buffer since the Co(111) single crystal grows on $MgB_2(0001)$ as well as on MgO(111). As shown in Fig. S6, for all temperatures, FMR spectra collected on $MgB_2(25)/Co(5)$ present a double resonance peak whose origin is still unclear. The damping extracted from the broadest resonance peak is insensitive to the Tc transition and is suppressed when decreasing the Co thickness down to 3nm. The doubling of α of all three samples when the temperature decreases from 300K to 2K (Fig. 3(b) and S6(b)) was previously correlated in the literature to its spin-orbit coupling amplitude and a change in K_{oop} with temperature [31,40,41]. Indeed, as shown in Fig. S2(b), M_{eff} extracted from FMR monotonically decreases by 0.3 T when the temperature is reduced from 300 K to 5K, whereas M_s measured by SQUID remains quite constant. The difference of α between MgB_2/Co(5) and MgO/Co(5) above T_c, is of the order of $5x10^{-3}$, i.e. 3 times smaller than in the case of $MgB_2/Ni_{80}Fe_{20}(5)$. It can be explained by the absence of intrinsic damping sample to sample variation since the RHEED images of the two epitaxial Co layer look very similar (Fig. S1). Moreover, based on eq. (2) and considering similar $g_{eff}^{\uparrow\downarrow}/t_F$ term, α_{sp} is also expected to be two times smaller for MgB_2/Co than for $MgB_2/Ni_{80}Fe_{20}$ since M_s for Co is twice the $Ni_{80}Fe_{20}$ one. Below Tc, α of MgB_2/Co reduces whereas α of the reference sample remain constant (Fig. 3(b)). In a previous report [14], the bad quality of the NbN/CoFe interface was suspected to foster the absence of Gilbert damping reduction below T_c. Here in epitaxial MgB_2/Co, the chemical and physical defects at the interface are limited and we observe the damping reduction. Still, although the intrinsic damping difference between MgB_2/Co(3) and MgO/Co(5) bilayers (Fig. 3(b) must be small and the spin pumping contribution must dominate, $\Delta\alpha^S$ remain small (about 10% similar to $Ni_{80}Fe_{20}$) as compare to the damping difference above Tc. Note that the relative amplitude of $\Delta\alpha^S$ is much larger in

Fig. S6c for MgB_2/Co(5) without clear explanation. More investigations are required to confirm or not that the superconductive gap opening fully suppresses the spin pumping contribution to the damping below Tc. Further systematic studies of how the decrease in the effective damping constant across Tc relies on the MgB_2 and F thicknesses are especially needed in the future.

To conclude, single crystalline MgB_2(0001) superconducting thin films, with thicknesses ranging from 1 nm to 91 nm, were grown by MBE on sapphire(0001)/MgO(111). Their critical temperature T_c is above 30K for all thicknesses larger than 15 nm and drops down to 2.5K for 5 nm thickness. The MgB_2 top surface, characterized by a good crystalline order with no pollution and a low roughness, allows to form a clean interface with epitaxial Co or polycrystalline $Ni_{80}Fe_{20}$ films. In both MgB_2/Co and MgB_2/$Ni_{80}Fe_{20}$, we observe a decrease of spin pumping into the MgB_2 layer when the superconducting gap opens. The present results show that MgB_2 thin films could be suitable to implement superconducting spintronic at 30K which is not only relevant for future technological development, but also relaxes experimental constraints related to low-temperature investigations.

Supplementary Material

It contains additional figures, including RHEED images and FMR data, that support the findings of the main text but which are not essential to understanding it.

Acknowledgements

The authors thank the CCMagCryo at Institut Jean Lamour for its help with the magnetic and FMR measurements, the CC X-gamma at Institut Jean Lamour for its help with the X-ray characterization, the CC3M at Institut Jean Lamour, for its help with TEM analysis. The work was supported by the « SONOMA» project co-funded by FEDER-FSE Lorraine et Massif des Vosges 2014-2020, a European Union Program, and by a government grant managed by the ANR as part of the France 2030 investment plan from PEPR SPIN ANR-22-EXSP 0008.

Refences

[1] F. S. Bergeret, A. F. Volkov, and K. B. Efetov, Phys. Rev. Lett. **86**, 4096 (2001).
[2] J. Linder and J. W. A. Robinson, Nature Phys **11**, 307 (2015).
[3] M. Eschrig, Physics Today **64**, 43 (2011).
[4] K. Ohnishi, S. Komori, G. Yang, K.-R. Jeon, L. A. B. Olde Olthof, X. Montiel, M. G. Blamire, and J. W. A. Robinson, Appl. Phys. Lett. **116**, 130501 (2020).
[5] C. H. L. Quay, D. Chevallier, C. Bena, and M. Aprili, Nature Phys **9**, 84 (2013).
[6] M. Inoue, M. Ichioka, and H. Adachi, Phys. Rev. B **96**, 024414 (2017).
[7] Y. Tserkovnyak, A. Brataas, and G. E. W. Bauer, Phys. Rev. Lett. **88**, 117601 (2002).
[8] T. L. Gilbert, IEEE Transactions on Magnetics **40**, 3443 (2004).
[9] S. S. Kalarickal, P. Krivosik, M. Wu, C. E. Patton, M. L. Schneider, P. Kabos, T. J. Silva, and J. P. Nibarger, J. Appl. Phys. **99**, 093909 (2006).
[10] C. Bell, S. Milikisyants, M. Huber, and J. Aarts, Phys. Rev. Lett. **100**, 047002 (2008).
[11] J. P. Morten, A. Brataas, G. E. W. Bauer, W. Belzig, and Y. Tserkovnyak, Europhys. Lett. **84**, 57008 (2008).
[12] K.-R. Jeon, C. Ciccarelli, A. J. Ferguson, H. Kurebayashi, L. F. Cohen, X. Montiel, M. Eschrig, J. W. A. Robinson, and M. G. Blamire, Nature Mater 17, 6 (2018)
[13] M. Müller, R. Hoepfl, L. Liensberger, S. Geprägs, H. Huebl, M. Weiler, R. Gross, and M. Althammer, Mater. Quantum. Technol. **1**, 045001 (2021).
[14] M. Müller, L. Liensberger, L. Flacke, H. Huebl, A. Kamra, W. Belzig, R. Gross, M. Weiler, and M. Althammer, Phys. Rev. Lett. **126**, 087201 (2021).
[15] S. J. Carreira, D. Sanchez-Manzano, M.-W. Yoo, K. Seurre, V. Rouco, A. Sander, J. Santamaría, A. Anane, and J. E. Villegas, Phys. Rev. B **104**, 144428 (2021).
[16] W. Tian, X. Q. Pan, S. D. Bu, D. M. Kim, J. H. Choi, S. Patnaik, and C. B. Eom, Appl. Phys. Lett. **81**, 4 (2002).
[17] T. P. Krinitsina, E. I. Kuznetsova, M. V. Degtyarev, and Yu. V. Blinova, Phys. Metals Metallogr. **122**, 12 (2021).
[18] C. Buzea and T. Yamashita, Supercond. Sci. Technol. **14**, R115 (2001).
[19] J. Nagamatsu, N. Nakagawa, T. Muranaka, Y. Zenitani, and J. Akimitsu, Nature **410**, 6824 (2001).
[20] P. C. Canfield and G. W. Crabtree, Physics Today **56**, 3 (2003).
[21] L. N. Cooper, Phys. Rev. Lett. **6**, 12 (1961).
[22] S. A. Wolf, S. B. Qadri, J. H. Claassen, T. L. Francavilla, and B. J. Dalrymple, J. of Vacuum Scie; & Techno. A: Vacuum, Surfaces, and Films **4**, 3 (1986).
[23] V. L. Ginzburg and L. D. Landau, *On the theory of superconductivity*, in Collected Papers of L.D. Landau (Elsevier, 1965), pp. 546–568.
[24] S. Patnaik, L.D. Cooley, A. Gurevich, A.A. Polyanskii, J. Jiang, X.Y. Cai, A.A. Squitieri, M.T. Naus, M.K. Lee, J.H. Choi, Supercond. Sci. Technol. **14**, 6 (2001).
[25] C. Zhang, Y. Wang, D. Wang, Y. Zhang, Z.-H. Liu, Q.-R. Feng, and Z.-Z. Gan, J. Appl. Phys. **114**, 2 (2013).
[26] S. Beguhn, Z. Zhou, S. Rand, X. Yang, J. Lou, and N. X. Sun, J. Appl. Phys. **111**, 07A503 (2012).
[27] D. M. Pozar, *Microwave Engineering*, 4th ed (Wiley, Hoboken, NJ, 2012).
[28] C. Kittel, *Ferromagnetic Resonance*, in *Introduction to Solid State Physics*, 8th ed (Wiley, Hoboken, NJ, 2005).
[29] M. A. W. Schoen, J. M. Shaw, H. T. Nembach, M. Weiler, and T. J. Silva, Phys. Rev. B **92**, 184417 (2015).
[30] B. Khodadadi, A. Rai, A. Sapkota, *et al.*, Phys. Rev. Lett. **124**, 157201 (2020).
[31] A. Brataas, Y. Tserkovnyak, and G. E. W. Bauer, J. Magn Magn. Mater. **272**, 1981 (2004).
[32] M. Tokaç, S. A. Bunyaev, G. N. Kakazei, D. S. Schmool, D. Atkinson, and A. T. Hindmarch, Phys. Rev. Lett. **115**, 056601 (2015).
[33] S. Martín-Rio, A. Pomar, Ll. Balcells, B. Bozzo, C. Frontera, and B. Martínez, J. Magn. Magn. Mater; **500**, 166319 (2020).
[34] G. Counil, T. Devolder, J.-V. Kim, P. Crozat, C. Chappert, S. Zoll, and R. Fournel, IEEE Trans. Magn. **42**, 3323 (2006).
[35] C. T. Boone, H. T. Nembach, J. M. Shaw, and T. J. Silva, J. Appl. Phys. **113**, 153906 (2013).
[36] J. Bardeen, L. N. Cooper, and J. R. Schrieffer, Phys. Rev. **108**, 1175 (1957).

[37] J.P. Morten, A. Brataas, G.E.W. Bauer, W. Belzig, Y. Tserkovnyak, Europhys. Lett. **84**, 57008 (2008)
[38] M. Inoue, M. Ichioka, H. Adachi, Phys. Rev. B **96**, 024414 (2017)
[39] Y. Yao, Q. Song, Y. Takamura, J.P. Cascales, W. Yuan, Y. Ma, Y. Yun, X.C. Xie, J.S. Moodera, W. Han, Phys. Rev. B 97, 224414 (2018)
[40] S. M. Bhagat and P. Lubitz, Phys. Rev. B **10**, 179 (1974).
[41] T.G.A. Verhagen, H.N. Tinkey, H.C. Overweg, M. van Son, M Huber, J.M. van Ruitenbeek and J. Aarts, J. Phys.: Condens. Matter 28 056004 (2016)